ADVANCED ENGINEERING MATERIALS

DOI: 10.1002/adem.201700319

A Microvascular System for the Autonomous Regeneration of Large Scale Damage in Polymeric Coatings**

By *Ryan C. R. Gergely, Michael N. Rossol, Sharon Tsubaki, Jonathan Wang, Nancy R. Sottos* and *Scott R. White**

Self-healing polymers are capable of self-repair either in response to the damage or through external stimuli, but are limited in their ability to autonomously control the volume of healing agents released, in the length scale of damage they address, and in their ability to respond to multiple damage events. Here, the authors report a novel design for healing agent storage and release for vascular coating systems that allows for complete regeneration of a coating with precise and autonomous control of coating thickness. A variety of healing agent formulations that cure under ambient sunlight are explored and their cure profiles and mechanical properties are reported. In the proposed vascular coating system, the stored healing agent remains stable within the network until large-scale damage (e.g., abrasion) completely removes the protective coating. A precise volume within the network is then released, and cures when exposed to simulated sunlight to reform the protective coating. This coating system facilitates consistent coating thickness and hardness for several cycles of coating removal and regeneration.

1. Introduction

The burgeoning field of self-healing materials offers the potential for synthetic materials that have biological-like responsiveness to repair themselves when damaged. The potential advantages of this approach in materials design is improved service lifetime and safety, as well as reduced overdesign typical in engineering structures.[1–3] Historically, research in self-healing polymers and composites has targeted damage due to scratches, fracture, delamination, and puncture.[4–9] No matter the type of healing system invoked (capsule-based, vascular, or intrinsic), nearly all are relegated to small scale damage modes.

Protective coatings shield the underlying substrate from harsh environmental conditions. Regular inspection and repair intervals are required to maintain protection – self-healing coatings aim to reduce or eliminate this required maintenance. Previous demonstrations of self-healing polymeric coatings have almost exclusively focused on cracks or scratch damage. In both microcapsule and microvascular systems, reactive fluids (healing agents) are released in response to damage.[7,8] When the scale of damage is small, healing agents can be drawn into the crack via capillary forces. Intrinsic systems are inherently reversible and reform bonds when there is intimate contact of the damage surfaces.[10,11] However, if the damage is sufficiently large, transport of the healing agent by capillary forces is inhibited, and reversible bonding is not possible due to the separation between damage surfaces. In addition, capsule based systems are limited both in their payload (total volume of healing agent) and they only allow for a single repair event.[7] In contrast, microvascular systems can deliver a potentially

[*] *Prof. S. R. White*
Department of Aerospace Engineering, Beckman Institute for Advanced Science and Technology, University of Illinois at Urbana-Champaign, Urbana, IL, 61801, USA
E-mail: swhite@illinois.edu
Dr. R. C. R. Gergely, S. Tsubaki
Department of Mechanical Science and Engineering, Beckman Institute for Advanced Science and Technology, University of Illinois at Urbana-Champaign, Urbana, IL, 61801, USA
Dr. M. N. Rossol, J. Wang, Prof. N. R. Sottos
Department of Materials Science and Engineering, Beckman Institute for Advanced Science and Technology, University of Illinois at Urbana-Champaign, Urbana, IL, 61801, USA

[**] *This work has been financially supported by the Air Force Office of Scientific Research (AFOSR, grant number, FA9550-16-1-0017). J. W. and S. T. were partially funded by the Illinois Space Grant Consortium Undergraduate Research Opportunity Program (UROP). We extend our gratitude to J. S. Moore for advice, insightful discussions, and expert opinion on the development of regenerative polymeric systems. We also thank C. B. Montgomery for his assistance with microscope imaging. (Supporting Information is available online from Wiley Online Library or from the author).*

inexhaustible supply of healing agents and they enable multiple repair events.[8,9,12] Introducing a pressurized microvascular system can overcome the limitations of capillary forces, as well as reduce the density of microvascular channels necessary to recover a given damage size.[4,5]

Recently, Gergely et al. utilized a pressurized delivery system with a microvascular healing approach to regenerate polymeric coatings in response to large scale abrasive damage.[12] A valve that blocked UV penetration into a vascularized substrate both protected the stored healing agent from premature curing and isolated the abrasive damage from the vascular network. This system utilized a one-part sunlight curable epoxy healing agent to eliminate the necessity for in situ mixing prevalent in self-healing systems.[6,9] Despite its success, one key limitation of the coating system was the requirement for external control to terminate the flow of healing agent during the regeneration event in order to avoid excessive bleed out.

A significat body of research has developed around light-healing systems that use a photochemical approach to induce repair.[13–19] Light-healing systems can potentially harness energy from sunlight to enable self-healing, thus requiring no human intervention. Various types of damage have been targetted by light-healable systems from scratches in coatings[13,14] to partial or complete fracture.[15–19] In contrast to existing light-healable coatings, this work targets complete abrasive removal of the coating that exposes the substrate, and uses commercially availible chemistries to formulate sunlight healing agents for coatings.

In this paper, we report on a novel storage and release mechanism for autonomous regeneration of polymer coatings. Our design relies on a pressure-activated membrane element (an "accumulator") that stores a prescribed volume of healing agent. Integration of the accumulator, as a localized reservoir in a microvascular network, eliminates the need for external control of healing agent delivery. We also consider three important factors in the design of a regenerative system: the relevant timescales of the regeneration cycle, modulation of these timescales, and tuning of the healing agent volume released. New sunlight curable healing agents are explored for both modulation of curing kinetics and mechanical performance. Factors affecting the volume of healing agents released and the timescale for their delivery are studied. The healing agent payload volume is calibrated by both experimental measurement and an analytical model. Multiple regeneration cycles of protective polymer coating with controlled thickness are demonstrated using a sunlight curable healing agent.

2. Results and Discussion

Our concept for regenerative coatings, is illustrated in Figure 1, for three distinct stages: trigger, transport, and repair. Upon removal of the coating by damage (trigger), the underlying vasculature is exposed and a prescribed volume of uncured liquid healing agent is released onto the surface of the substrate (transport). Ultraviolet (UV) light from the sun cures the healing agent, reforming the protective coating (repair).

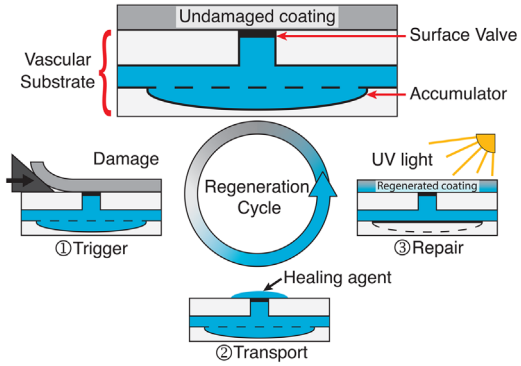

Fig. 1. Coating regeneration cycle and design. (1) Coating damage and removal triggers the release of liquid healing agent stored in the underlying vasculature. (2) Embedded accumulator releases a prescribed volume of healing agent to the surface. (3) A one-part healing agent reforms the protective coating when exposed to simulated sunlight. The surface valve protects the unreacted healing agent stored within the vascular substrate by blocking UV penetration.

2.1. Specimen Design

The release of a prescribed volume of healing agent is accomplished by the synergistic operation of two key components: the surface valve and the accumulator (Figure 2). These components are positioned below the coating in a multilayer structure similar to skin. A fully integrated surface valve resides at the interface between coating and substrate, isolating the uncured healing agent from the coating (Figure 2a and b). Incorporating 0.5 wt% carbon black into the compliant (poly(dimethylsiloxane), PDMS) surface valve effectively prevents the penetration of UV light into the underlying vascular substrate. In response to coating removal, pressure within the accumulator opens the valve, releasing healing agent to the damage surface. The accumulator (Figure 2c) stores a specified volume of healing agent dictated by the internal pressure. When the coating is intact, the valve is closed and constrained by the coating. The accumulator, however, is free to deflect with the magnitude of the deflection dependent on the geometry, material properties, and system pressure. In order to properly design the coating system, the various timescales associated with the coating regeneration cycle, as well as the parameters controlling the volume of healing agent released were examined.

2.2. Regeneration Timescales

The interactions between the timescales within the regeneration cycle (i.e., those related to trigger, transport, and repair) must be considered collectively in the design of a self-healing system. Figure 3 shows how the relevant timescales are related to the accumulator pressure and coating hardness. All of these timescales start immediately after damage triggers the healing response. The time required to transport healing agent from its quiescent state in the substrate to the site of damage is transport time ($t_{transport}$). The healing agent begins to react once released and exposed to UV light, and then solidify at the gel time (t_{gel}). Hardness will continue to increase with the passage of time until the coating is fully repaired (t_{repair}). At this point, the accumulator can

ADVANCED ENGINEERING MATERIALS 2017,
DOI: 10.1002/adem.201700319

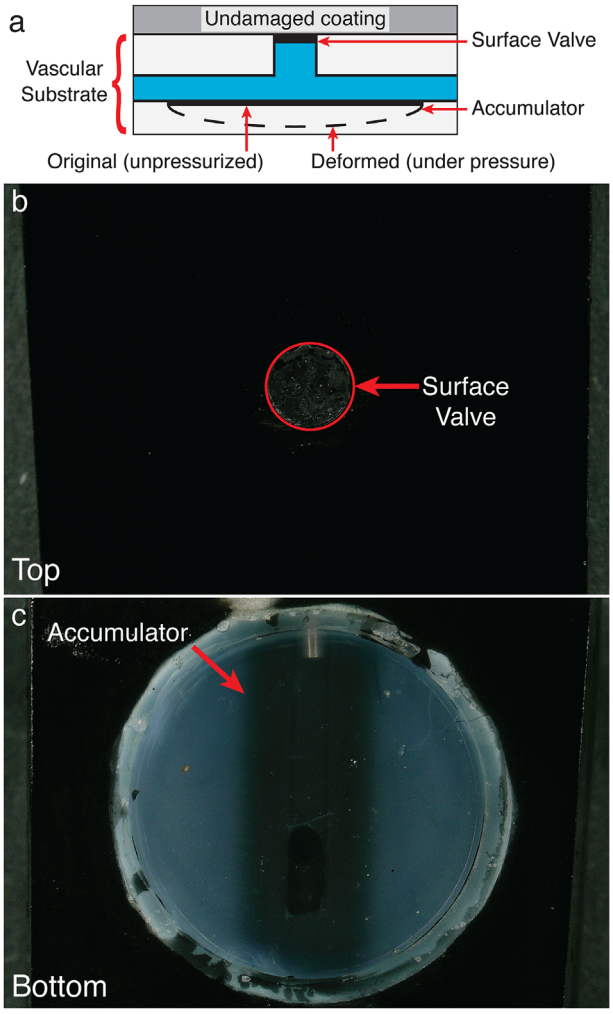

Fig. 2. Accumulator-surface valve design and prototype. (a) Cross-sectional diagram of accumulator-valve showing unpressurized and pressurized configuration. Membrane deflection enables volume storage. (b) Top and (c) bottom images of accumulator-valve prototype (scale bar = 5 mm).

once again be charged ($t_{recharge}$) in anticipation of the next damage event.

The most conservative design requires the complete release of the healing agent payload prior to gelation ($t_{transport} < t_{gel}$). In addition, to sustain re-pressurization of the vascular substrate without damage to the coating (e.g., debonding), the repair time should be less than the recharge time ($t_{repair} < t_{recharge}$). The curing kinetics of the healing agent chemistry dictate the time required to gel (t_{gel}), and the time required to fully cure the coating (t_{repair}). The system geometry, material properties, and fluid viscosity all influence the transport time ($t_{transport}$), while recharge time ($t_{recharge}$) is externally controlled. The optimal design can be obtained by tuning the chemistry, geometric parameters, and material properties of the entire coating system.

2.3. UV Curable Healing Agents

The viscosity and curing kinetics of the healing agent used for coating regeneration will influence the transport, gel, and repair times for the system. We examined three formulations, spanning the breadth of available sunlight (UV) curable

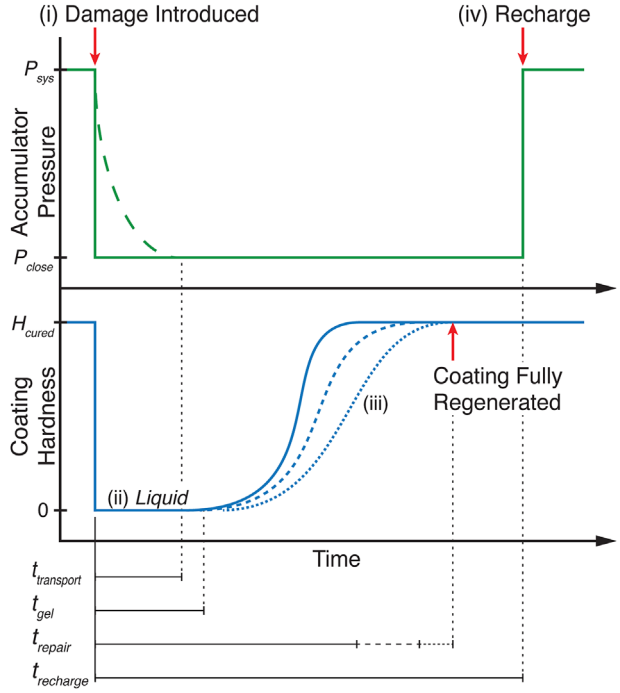

Fig. 3. Coating system response after a damage event. (i) Damage event removes coating, triggering the release of the stored healing agent. Pressure in the accumulator drops to a level where the surface valve closes over a timescale of $t_{transport}$. (ii) The released healing agent remains liquid until gelation occurs (t_{gel}). (iii) The hardness of the coating increases after gelation until coating is fully cured (t_{repair}). (iv) The accumulator is subsequently recharged (pressurized) in preparation for subseqent damage events ($t_{recharge}$).

chemistries[20]: (i) a radical initiated thiol-ene formulation (TATATO:PETMP, 0.1 wt% DMPA photoinitiator, 0.03 wt% Q1301 inhibitor),[21,22] (ii) a radical initiated acrylate formulation (TMPTA, 3 wt% Irgacure 184 photoinitiator), and (iii) a cationic initiated epoxy formulation (Epon 813, 4 wt% Irgacure 250 photoinitiator).[12] The chemical structures of the healing agent constituents can be found in Figure S1. The viscosities of the three candidate healing agents are given in Table 1, and are similar to previous healing agents used in microvascular systems.[4,6,9]

The gel time (t_{gel}) of candidate sunlight curable healing agents was determined by characterizing the cure depth (C_d)[23]:

$$C_d = D_p log\left(\frac{E_{max}}{E_c}\right) \quad (1)$$

where E_{max} is the dose of UV light ($E_{max} = It$, where I = irradiance, t = time), D_p is the penetration depth, and E_c is the critical dose. Both D_p and E_c are characteristic parameters of the chemical formulation and are directly related to the cure kinetics.

The cure depth (C_d) was determined by measuring the resulting thickness of gelled material after exposing the three candidate healing agents to controlled doses of simulated sunlight (365 nm, 0.25 or 1 mW cm^{-2}, Figure S2,S3).[24,25] Importantly, the difference between the simulated and the

DOI: 10.1002/adem.201700319

Table 1. Characteristics of three sunlight curable healing agent formulations

Formulation	Viscosity [cP]	Penetration depth, D_p[μm]	Critical dose, E_c[mJ cm^{-2}]	Time required (t_{gel}) for cure depth, $C_d = 1$ mm at 1 mW cm^{-2}	Vickers hardness, HV [12 h at 1 mW cm^{-2}]
Radical Thiol-Ene	430	4150 ± 300	11 ± 1	14.0 ± 1.0 s	–
Radical Acrylate	130	610 ± 11	10.9 ± 0.1	56.1 ± 1.4 s	24.4 ± 1.5
Cationic Epoxy	1020	1180 ± 23	925 ± 1	36.0 ± 0.6 min	17.8 ± 0.2

Error represents the standard deviation between two measurements for cure depth tests (D_p, E_c, t_{gel}), and five measurements for hardness tests.

actual sunlight in both the intensity and the spectrum will effect the cure time. Cure depth is plotted against dose (E_{max}) in Figure 4a (raw values are given in Table S1–S3). D_p and E_c were calculated for each formulation (Table 1) by fitting Equation 1 to the data in Figure 4a. Depth of penetration (D_p) was highest for the thiol-ene formulation ($D_p = 4150$ μm), followed by the epoxy formulation ($D_p = 1080$ μm), while the acrylate formulation had the lowest value ($D_p = 610$ μm). The critical doses (E_c) of both radical initiated formulations (thiol-ene and acrylate) are comparable ($E_c \approx 11$ mJ cm^{-2}), while the cationic epoxy formulation requires a much larger dose for any gelation to occur ($E_c = 925$ mJ cm^{-2}). Using the obtained values for D_p and E_c, the required dose for the target coating thickness of 1 mm was calculated for simulated sunlight ($I = 1$ mW cm^{-2}). The gel time ($t_{gel} = E_{max}/I$) was then calculated as 14 s, 56 s, and 36 min for the thiol-ene, acrylate, and epoxy formulations, respectively.

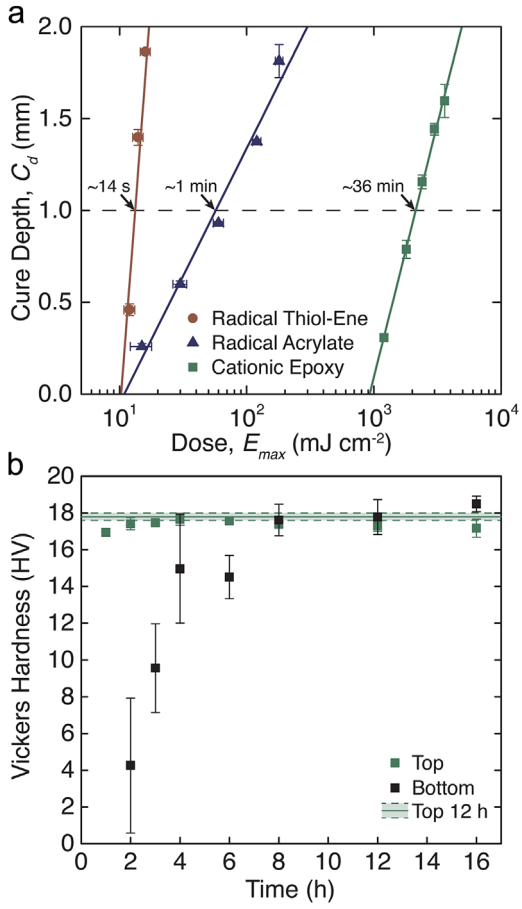

Fig. 4. Cure and hardness characterization of candidate healing agents. (a) Cure depth as a function of dose of simulated sunlight (365 nm, 1 mW cm^{-2}). Note: cure depth error bars represent one standard deviation of five measurements. Dose error bars represent estimated error based on variation in lamp intensity and exposure time. (b) Vickers hardness as a function of exposure time (365 nm, 1 mW cm^{-2}) for cationic epoxy system based on mesurement of the top and bottom of a ≈1 mm thick coating. Note: Error bars represent one standard deviation of three tests. Discrete datapoints reproduced from ref.[12]

The mechanical properties required by the final application will also influence which healing agent formulation is appropriate. The hardness of each candidate system was measured after full UV cure (12 h, 1 mW cm^{-2}, Table 1). The acrylate and epoxy formulations reached a hardness of 24.4 ± 1.5 HV and 17.8 ± 0.2 HV, respectively, by Vickers indentation testing. The thiol-ene system was soft when fully cured and could not be measured.

After the healing agent has fully cured (t_{repair}), the system can once again be pressurized or recharged ($t_{recharge}$) in anticipation of the next damage event. Of the three formulations, the epoxy formulation has the slowest cure kinetics, thus it sets an upper bound on the recharge time ($t_{recharge}$). In our previous investigation, the epoxy formulation was selected for further characterization.[12] The results indicated that after 8 h of exposure to the simulated sunlight lamp, the epoxy coating is fully regenerated in terms of hardness (Figure 4b) and is also ≈100% cured, as confirmed by differential scanning calorimetry (DSC). We note that the coating hardness is not influenced by the substrate.[12] The candidate healing agents identified offer a wide range of cure kinetics, viscosities, and hardnesses; enabling a great deal of flexibility for tailoring the regenerative coating system for target applications.

2.4. Healing Agent Release Profile

The valve geometry governs the timescale over which the healing agent payload is released ($t_{transport}$). The payload release profile (pressure vs. time) was measured for a variety of specimen designs using glycerol as the test fluid in order to avoid swelling of the valve due to absorption (Figure 5a). The transport time ($t_{transport}$) is defined as the time at which the rate

DOI: 10.1002/adem.201700319

ADVANCED ENGINEERING MATERIALS

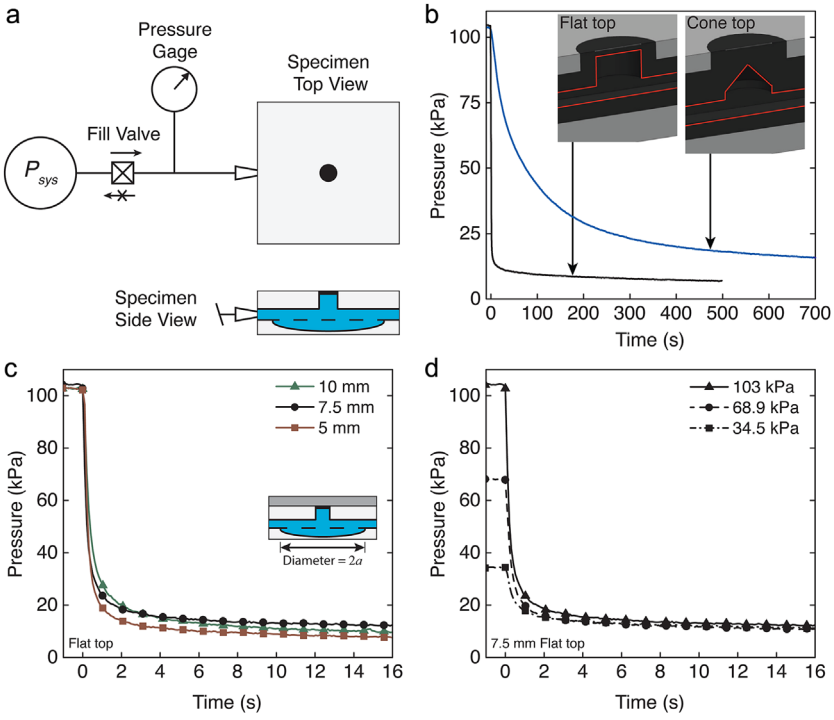

Fig. 5. Payload release profile evaluation ($t_{transport}$). (a) Schematic of specimen charging and pressure monitoring scheme. (b) Pressure decay profile during volume relase for flat top and cone top valve geometries (7.5 mm diameter accumulator). (c) Pressure decay profiles for three accumulator diameters with flat top valves. (d) Pressure decay profile for three system pressures with 7.5 mm diameter accumlator and flat top valve. Note: Glycerol was used as the test fluid for all experiments.

of change in pressure decays within 20 times the equilibrium plateau bleed rate (Figure S4). For the release experiments, the surface valve was artificially constrained by a piece of adhesive tape and the accumulator was charged to the target pressure (P_{sys}). After equilibrating the system, the constraint (adhesive tape) was removed and accumulator pressure was monitored with time (Figure 5b–d).

The effect of valve geometry on transport time was investigated by testing both flat and cone top designs (Figure 5b). Valves are constructed of a flexible silicone elastomer (poly(dimethylsiloxane), PDMS) loaded with 0.5 wt% carbon black. Both valve geometries employ a slit-type opening that dilates under pressure. The flat top design exhibits a rapid release of the healing agent ($t_{transport} < 10$ s), while the cone top valve shows a much slower response ($t_{transport} > 700$ s).

For conservative designs that require $t_{transport} < t_{gel}$, the flat top design satisfies this requirement for all three candidate healing agents explored in this study. The significantly longer transport time for the cone top valve could result in curing of the healing agent prior to complete payload delivery, reducing the maximum potential coating thickness and future valve operation. For this reason, the flat top geometry (with $t_{transport} < t_{gel}$ for all three candidate healing agents) was used exclusively during the remainder of this study.

The effect of the accumulator diameter (5, 7.5, and 10 mm) on the transport time is presented in Figure 5c. The payload release profiles for all three accumulator diameters are comparable, indicating $t_{transport}$ is relatively independent of the accumulator geometry. The payload release profiles for the 7.5 mm diameter accumulator were measured for three different pressures (34.5, 68.9, and 103 kPa) (Figure 5d). The transport time ($t_{transport}$) is, again, relatively insensitive to system pressure. Consequently, the payload volume can be tuned by changing the accumulator geometry and system pressure without influencing the transport time.

2.5. Payload Volume

The key advancement detailed in this work is the accumulator, which is capable of locally storing a prescribed volume of healing agent for autonomic release in response to damage (Figure 2c). The accumulator consists of a flexible elastomeric membrane (PDMS) that deforms under pressure. Understanding the correlation between system pressure and stored volume will facilitate control of the thickness of the regenerated coating. Payload volume was experimentally measured using 3D-digital image correlation (3D-DIC) and mass measurements. An analytical model was also developed and validated using these experimental measurements.

2.5.1. Experimental Measurement

3D-DIC was implemented to capture the deformation of the accumulator (Figure 6). Pressures were applied in a stepwise fashion (6.9 kPa steps from 6.9 to 69 kPa, 17.2 kPa steps from 86 to 207 kPa) and images were collected from two cameras focused on the accumulator. 3D-DIC facilitated the measurement of the full field displacements in three dimensions yielding the deformed accumulator shape,

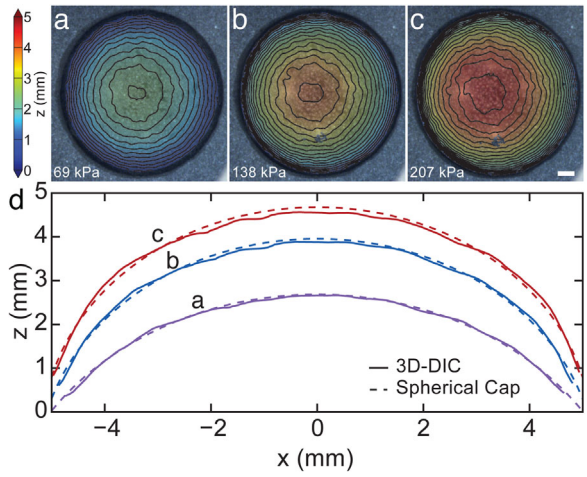

Fig. 6. Contour plots of deflection measured by 3D-DIC for 10 mm diameter accumulator at pressures of (a) 69 kPa, (b) 138 kPa, and (c) 207 kPa. (d) Line scans of accumulator surface profiles from (a–c) (scale bar = 1 mm).

DOI: 10.1002/adem.201700319

FULL PAPER

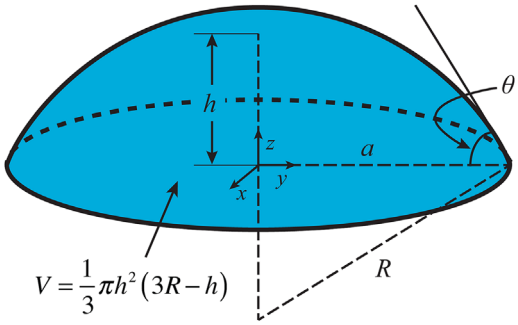

Fig. 7. Schematic of spherical cap with relevant dimensions.

illustrated by the contour plots in Figure 6a–c. The volume stored within the accumulator is determined by the difference between the undeformed (flat) and the deformed state of the accumulator. The accumulator's surface topography is best represented as a spherical cap with volume described by refs.[26,27]:

$$V = \frac{1}{3}\pi h^2(3R - h) \tag{2}$$

where R is the radius of the sphere and h is the height of the cap (Figure 7). Line scans of the surface topography from 3D-DIC and the corresponding spherical fit for pressures of 69, 138, and 207 kPa are shown in Figure 6d. The calculated volume as a function of pressure for the three accumulator geometries is shown in Figure 8a.

The volume of fluid released was also measured as a function of pressure (Figure 8b). For these experiments, the surface valve was artificially constrained (with a rubber stopper) and the accumulator was charged to a target pressure. After equilibration, the constraint was removed and the stored fluid was released. Pressures were applied in 35.5 kPa steps up to 207 kPa for two specimens, or until the specimen failed. In all cases, the released volume was slightly less than stored volume (as measured by 3D-DIC). When the payload is released, the pressure drops rapidly to a plateau value when the surface valve closes, that is, the closing pressure ($p_{close} = 9 \pm 4$ kPa, Figure 5). Subtracting the unreleased volume (corresponding to $P = 9$ kPa) from the stored volume calculated by 3D-DIC (4–44 μL, depending on accumulator diameter) gives good agreement between both experimental measures of volume and the analytical model (Figure 7c,S4).

2.5.2. Analytical Model

An analytical model was formulated to gain insight into the underlying mechanisms that dictate the relationship between stored volume and pressure. The model is derived from that of a thin-walled spherical balloon with rubber elastic behavior, extended here to the assumed spherical cap geometry.[28,29] The assumptions of the model are: (i) the wall is thin, implying the accumulator does not resist bending and stresses are uniform through the thickness; (ii) deformation maintains spherical symmetry, with the stresses independent of the position on the accumulator; and (iii) edge effects are neglected.[30] As in the case for a spherical balloon,[28–30] the stresses in the plane of the accumulator were approximated as equibiaxial:

$$\sigma = \sigma_{11} = \sigma_{22} = \frac{pR}{2t} \tag{3}$$

where σ_{11} and σ_{22} are the in-plane stresses (true stress), p is the internal pressure, R is the radius of the sphere, $t = t_0/\lambda^2$ is the deformed thickness, t_0 is the undeformed thickness, and λ is the in-plane stretch ratio. The in-plane stretch ratio was estimated based on geometry (Figure 7):

$$\lambda = \frac{2R\theta}{2a} = \frac{R}{a}\sin^{-1}\left(\frac{R}{a}\right) \tag{4}$$

where $2R\theta$ is the deformed length, and $2a$ is the undeformed length.

$$R = \frac{a^2 + h^2}{2h} \tag{5}$$

where a is the initial accumulator radius, and h is the height of the spherical cap.

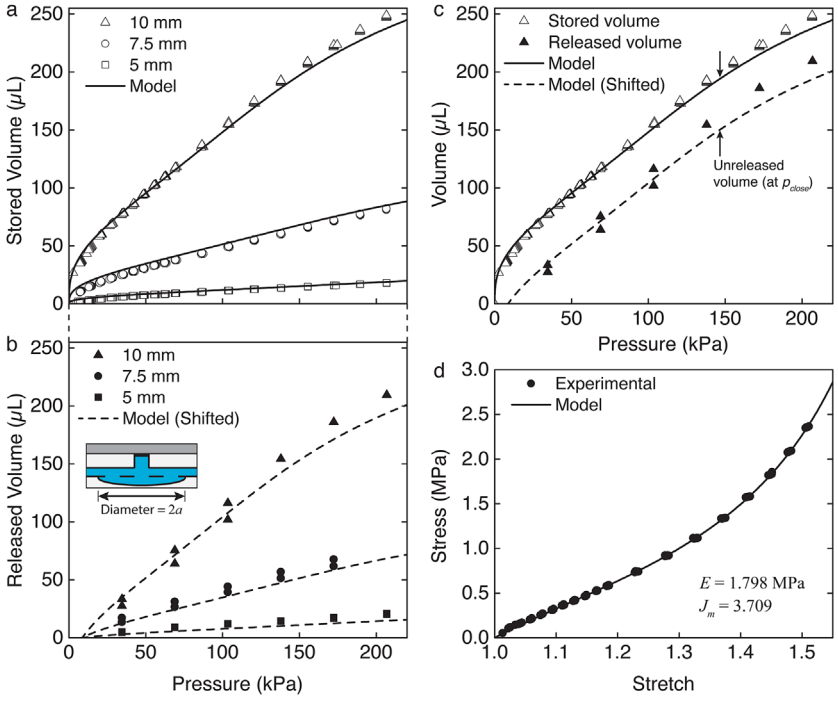

Fig. 8. (a) Stored volume extracted from 3D-DIC data (discrete datapoints) for each accumulator diameter, and analytical model (solid lines). (b) Released volume results from collecting and weighing the fluid volume released for a given pressure (test fluid = glycerol, discrete datapoints, n = 2), and analytical model (dashed lines). (c) Correction for unrelased volume associated with closing pressure (p_{close}) for 10 mm diameter accumulator. (d) Stress–stretch results extracted from 10 mm 3D-DIC experiment and equibiaxial model.

ADVANCED ENGINEERING MATERIALS 2017,
DOI: 10.1002/adem.201700319

ADVANCED ENGINEERING MATERIALS

We sought an appropriate constitutive relation to represent the rubber elastic stress–stretch behavior of the PDMS elastomer used to fabricate the accumulator. The pressure-height (volume) data calculated from 3D-DIC for the 10 mm diameter accumulator was converted to stress and stretch (Scheme S1). Stretch was calculated from the height (h_e) using Equations 4 and 5 with the initial accumulator radius (a), and stress was calculated from the pressure (p_e) using Equation 3. The material behavior was found to be well captured by the Gent model[31]:

$$\sigma = \frac{E}{3}\left(\lambda^2 - \lambda^{-4}\right)/\left[1 - J_1/J_m\right] \quad (6)$$

where E is the small strain elastic modulus, J_m is the stiffening parameter, and $J_1 = 2\lambda + \lambda^{-4} - 3$ is the first strain invariant.[32]

The material properties (E and J_m) were determined by fitting Equation 6 to the stress–stretch data (Figure 8d). Using the calibrated material properties (E and J_m) and the geometry (a and t_0), the analytical model was applied to predict the pressure–volume relationship for all three accumulator diameters (Figure 8a,b). Since it is not possible to write an explicit expression for volume in terms of pressure, the relationship was determined by sweeping though appropriate values of h and solving for R, V, λ, σ, t, and p using Equations 2–6 (Scheme S2).

A comparison of the experimentally measured and predicted volume–pressure relationships for the three accumulators are shown in Figure 8a and b. While the model slightly overpredicts the stored volume (from 3D-DIC), this limitation can be attributed to the assumption that the accumulator is thin. A commonly cited limit for thin membrane theory is $r/t > 10$,[30] however, the three geometries tested here correspond to $r/t = 5$, 7.5, and 10. Nevertheless, the simplicity of the model reveals the functional form of the volume–pressure relationship and remarkably accurate predictions are obtained. The circular membrane geometry facilitates the rapid increase in volume with pressure, and at higher pressures the constitutive response of the material limits the inflation of the accumulator (Figure 8d). Accurate prediction of the stored volume enables control of the regenerated coating thickness.

2.6. Coating Regeneration

Regeneration of a protective coating was demonstrated in response to large-scale coating damage and removal using the proposed accumulator-surface valve system. Damage was introduced by lifting the cured coating from the substrate, triggering the release of the stored liquid healing agent. The process of coating removal and regeneration was repeated for a total of four cycles (generations 1–4). The Vickers indentation hardness and coating thickness were measured to evaluate the efficacy of each regeneration cycle. Full regeneration to the same material properties as the original coating occurred after every cycle, indicated by the consistency in hardness (Figure 9a). Some variability in the

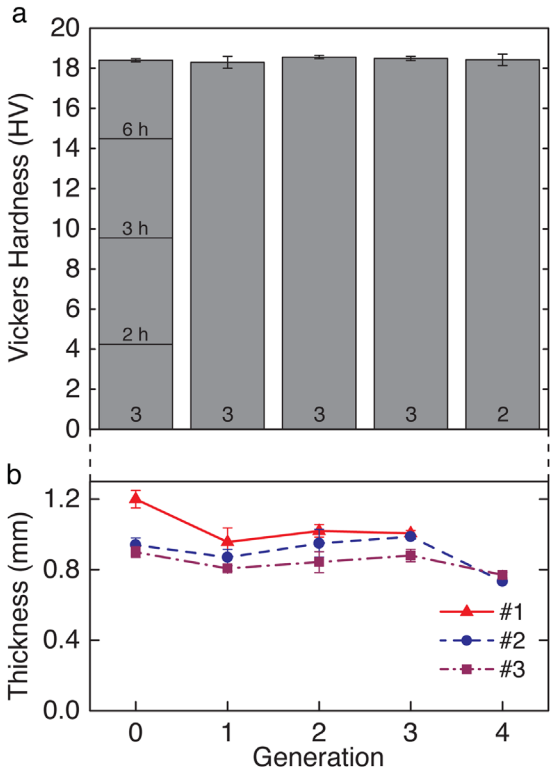

Fig. 9. Autonomous regeneration of epoxy coating. (a) Vickers hardness of each generation of coating, cured with simulated sunlight lamp (1 mW cm^{-2}, 12 h). Horizontal lines on generation 0 column indicate Vickers hardness of coating bottom at given time point (from Figure 4b). Note: Total number of specimens indicated at the base of the column. (b) Coating thickness measured for each generation for three specimens. Note: Error bars indicate one standard deviation of the data.

regenerated coating thickness was observed from cycle to cycle (Figure 9b). This variation was attributed to incomplete coating removal and/or loss of healing agent during coating removal.[33] Despite the variability, the coating thickness for a given specimen was maintained within ≈20% of the virgin thickness for all generations.

3. Conclusions

In this work, a novel design for healing agent storage and release for vascular coating systems that enables autonomic regeneration in response to coating damage is presented. The accumulator, a volume control element consisting of a flexible membrane, was coupled with a protective surface valve in order to demonstrate regeneration of a coating after large-scale damage. The timescales relevant to our regenerative strategy were explored, as well as methods for modulation of the rates of transport, release, and curing. Three different one-part sunlight curable healing agents were evaluated with gel times ranging from 14 s to 36 min. Factors affecting the payload release profile were examined, and it was established that the payload volume could be controlled without affecting the transport time. The payload volume was measured experimentally and an analytical model was developed using membrane theory and showed good agreement. We show four successive regenerations of a ≈1 mm thick polymer

DOI: 10.1002/adem.201700319

coating with full restoration of coating hardness. We envision the autonomous storage and release motif could be extended to other multifunctional systems, where fluidic volume control is required from self-healing[1] to thermal regulation.[34]

4. Experimental Section

4.1. Materials

Unless otherwise noted, materials were used as received. Thiol-ene was formulated as a stoichiometric mixture of triallyl-1,3,5-triazine-2,4,6-(1H,3H,5H)-trione (TATATO) and pentaerythritol tetra(3-mercaptopropionate) (PETMP) with 0.1 wt% 2,2-dimethoxy-2-phenyl-acetophenone (DMPA) photoinitiator and 0.03 wt% aluminum N-nitroso-N-phenylhydroxylamine (Q1301, Wako Specialty Chemicals) inhibitor. Acrylate was formulated as a mixture of trimethylolpropane-triacrylate (TMPTA) and 3 wt% 1-hydroxycyclohexyl phenyl ketone (Irgacure 184, BASF) photoinitiator. Epoxy was formulated as a mixture of EPON 813 (Diglycidyl ether of bisphenol-A (DGEBA) diluted with o-cresyl glycidyl ether (CGE)) and 4 wt% Iodonium, (4-methylphenyl)[4-(2-methylpropyl) phenyl]-, hexafluorophosphate (1-) (Irgacure 250, BASF) photoinitiator. TATATO, PETMP, DMPA, and TMPTA were obtained from Sigma Aldrich. The chemical structures of the healing agent constituents can be found in Figure S1. Viscosities were measured on a TA instruments AR-G2 rheometer using 25 mm aluminum parallel plates at room temperature (RT ≈ 21 °C).

4.2. Specimen Fabrication

The valve and vascular channel were made of PDMS (Sylgard 184, Dow Corning) containing 0.5 wt% carbon black (Vulcan XCR72R, Cabot Corporation). PDMS was molded in a 2-sided aluminum mold (Figure S6) and partially cured (16 min at 80 °C). This produced a PDMS valve attached to a channel with one open side. The channel was closed by bonding to a 0.5 mm thick sheet of PDMS (cured 16 min at 80 °C), using a film of uncured PDMS as a glue.[35] Multiple valve-channel components were bonded to a single sheet and partially cured (≈16 h at RT, 16 min at 80 °C). PDMS valve-channel components were then separated. A small hole (≈1 × 1 mm) was then cut in the channel on the opposite side to the valve. Accumulator elements of three diameters (5, 7.5, and 10 mm, PDMS no carbon black) were molded in 2-sided aluminum molds (Figure S7). The undeformed thickness of the accumulator (t_0) is 0.5 mm. The molds were compressed with a weight (1.84 kg) to constrain thickness. The PDMS was partially cured for 16 min at 80 °C. Accumulators were bonded to the PDMS valve-channel component on the side with the ≈1 × 1 mm hole using a film of uncured PDMS as a glue. The hole provided a connection between the accumulator and valve. The combined PDMS accumulator-valve-channel component was then fully cured (≈16 h at RT, 3 h at 80 °C). After curing the PDMS component, a 25 × 25 × 1 mm epoxy square with a circular hole of diameter corresponding to the accumulator was attached to the accumulator with a cyanoacrylate adhesive (Loctite® Super Glue Gel Control™, Henkel). The valve side of the specimen was then placed in contact with a glass slide (coated with release agent, Frekote 55-NC, Henkel) to create a sandwich structure (Figure S8). Six specimens were placed in a single weigh boat that served as a mold. Liquid epoxy (EPON 813, 22.7 pph EPIKURE 3300, Momentive, with 0.5 wt% carbon black) was poured into the mold to embed the sandwich structure and then cured (24 h at RT, 6 h at 80 °C). The multiple molded specimens were then sectioned to create single accumulator-valve specimens. The glass slide was removed to expose the top surface of the valve. A 1.5 mm long razor blade was used to pierce the top of the valve and create the valve opening. Connection of the source fluid to the specimen was made with a Luer-lock type stainless steel dispensing tip. A syringe needle (23 gauge) was used to pierce a hole in the end of the channel, and the larger dispensing tip (20 gauge, Nordson EFD) was attached with 5 min® epoxy (Devcon).

4.3. Cure Depth

The experimental setup consisted of a longwave UV source which simulated sunlight (365 nm, 0.25, or 1 mW cm^{-2}, Figure S2b, 25W Cole-Parmer UV Transilluminator), a photomask which created isolated areas exposed to the incident light, and the candidate sunlight curable healing agent confined between two glass slides separated by a 2 mm thick silicone gasket (Figure S3). The glass slides for acrylate and epoxy formulations were surface functionalized with a silane coupling agent to promote adhesion. To functionalize the surface, glass slide substrates were cut into 1 cm squares and cleaned in Piranha solution (3 H_2SO_4:1 H_2O_2 by volume, H_2O_2 was 30 w/w% in H_2O) at 120 °C for 60 min. The substrates were then rinsed with deionized water, dried with compressed air, and further dried in an oven at 120 °C for ≈10 min. The substrates were then immersed in a solution of toluene (ACS certified, Fisher Scientific) containing 20 mM silane (3-(trimethoxysilyl) propyl methacrylate or (3-glycidyloxypropyl) trimethoxysilane for acrylate and epoxy formulations, respectively, Sigma Aldrich). After 24 h, the substrates were sequentially rinsed with toluene, isopropanol, and deionized water, and dried with compressed air. The photomask consisted of a chrome coated glass substrate with a 5 × 5 array of squares, 2 × 2 mm each. Using a manual sliding shutter, the candidate sunlight curable healing agents were exposed to controlled doses of simulated sunlight. The dose was controlled via the exposure time and irradiance (10 s to 60 min, 365 nm, 0.25 or 1 mW cm^{-2}, Table S1–S3). Irradiance was verified with a UV light meter (UV513AB, General). Photopolymerization of the candidate healing agents results in propagation of a solid front into the well of fluid where the material is not masked. Five posts in one row were formed for each of five exposure times during a single experimental run. After UV exposure, the posts were developed with a solvent rinse (acetone) and gentle blowing with compressed air. To facilitate measurement of the post heights (cure depth, C_d) using a digital micrometer (Mitutoyo), the gel-like posts were exposed to a higher dose to increase cure (≈3.5 mW cm^{-2}, 30 min). Two experimental runs were performed on each candidate sunlight curable healing agent to check for consistency. The data reported in Figure 4a represents the average of five measurements from a single experimental run with the cure depth error bars representing one standard deviation, and dose error bars representing the estimated error in dose. The error in dose is a combination of the variability in irradiance (from lamp and slide thickness ≈6%), and error in exposure time (taken to be 2 s).

4.4. Payload Release Profile

The internal pressure of the accumulator-valve specimens was monitored to observe the time response of healing agent release. Specimens were attached to a fluid reservoir, as shown in the test configuration in Figure 5a. The surface valve was manually constrained (by applying a piece of adhesive tape to the surface of the specimen). The desired system pressure (P_{sys}) was supplied to the specimen to charge the accumulator. The system was allowed to equilibrate for 1 min. The fill valve was then closed. The pressure was

ADVANCED ENGINEERING MATERIALS 2017,
DOI: 10.1002/adem.201700319

monitored continuously as the constraint was removed from the surface valve and healing agent was released onto the surface of the substrate. While the flat top valves reach a plateau in pressure quickly, long times lead to slow decay of the remaining pressure due to leakage through the valve. Thus the closing pressure (p_{close}) was taken to be the measured pressure after 3 min. The transport time ($t_{transport}$) was defined as the time at which the rate of change in pressure decays within 20 times the equilibrium plateau bleed rate (Figure S4). For the flat top valve $t_{transport} = 6.9 \pm 1.5$ s. Glycerol was used for these experiments to ensure non-reactivity. The viscosity of glycerol is 890 cP, which is comparable to the both healing agents used in this study (Table 1) and those used in previous studies.[4,6,9]

4.5. 3D-Digital Image Correlation (3D-DIC)

Measurement of full-field displacements via digital image correlation (DIC) was accomplished by applying a speckle pattern to the specimen surface. High contrast speckles were produced using an airbrush (Badger No 150, Badger Air-Brush Co., Franklin Park, IL) with first white, then black, water-soluble paint. Images for DIC were taken using two digital cameras (Basler A631fc, Balser, Germany), each with a CCD resolution of 1388×1038 pixels and 180 mm lens (Tamron SP Di AF 180 mm F/3.5 Macro, Tamron Co., Japan). Images were taken at a magnification of 12 μm pixel^{-1}, the aperture setting was F-32, and the angle between the cameras was 16°. Image correlation was carried out using Vic-3D software (Correlated Solutions, Columbia, SC). The spatial resolution of the displacement measurement was maximized by choosing the smallest possible subset size, h_{sub}, that ensured full correlation ($h_{sub} = 45$ pixels or 540 μm).[36] The step size was selected to be $h_{step} = 4$ pixels (approximately $h_{sub}/10$). Incremental correlation was used to capture the large deformations experienced by the specimens during testing.

The accumulator's volume was calculated as a function of pressure by fitting a sphere to the accumulator's surface topography, as measured by DIC:

$$R^2 = (x - x_0)^2 + (y - y_0)^2 + (z - z_0)^2 \tag{7}$$

where (x_0, y_0, z_0) is the coordinate of the sphere's center, and (x, y, z) are the DIC coordinates of the accumulator surface. By adjusting the accumulators original position to the x-y plane, the height of the cap h can be calculated as $h = R + z_0$. Stored volume was calculated using Equation 2. The error in the calculated volume was estimated based on the discrepancy between the piece-wise integrated volume under the DIC and fitted surfaces:

$$\delta V = \sum \delta x \delta y \delta z \tag{8}$$

where δx and δy are the distances between data points, in x and y directions, respectively, and $\delta V = \sqrt{(z_{DIC} - z_{sphere})^2}$. To facilitate the calculation of δV, the DIC data was re-mapped onto a uniform x-y array with equal spacing to the original nodal spacing h_{step} by point-to-point interpolation. Thus:

$$\delta V = h_{step}^2 \sqrt{\sum (z_{DIC} - z_{sphere})^2} \tag{9}$$

for all available DIC data points δV as a function of pressure is shown in Figure S9.

4.6. Released Volume Testing

The method for released volume testing was analogous to the payload release profile experiments. However, the pressure gage was removed to eliminate any extra stored volume that could lead to falsely high volume release, and a rubber stopper was used to manually constrain the surface valve. Specimens were charged for 1 min at the desired system pressure (P_{sys}), and the released volume was collected and weighed after 3 min.

4.7. Regeneration Testing

Prior to testing, accumulator-valve specimens were charged with healing agent (Epon 813, with 4 wt% Irgacure 250) manually. The flat top valve geometry with a 10 mm diameter accumulator was used for all regeneration tests. An adhesive backed silicone sheet ($20 \times 20 \times 1$ mm thick, McMaster-Carr) with an 11 mm diameter hole was affixed to the top surface of the specimen and served as a well to contain the release volume of healing agent. Specimens were fixed to a 4-axis stage (Thor Labs) and leveled. To generate the virgin coating (generation 0), a tool with a silicone stopper was used to constrain the surface valve. A static pressure (97 kPa) was then applied to the specimen for 1 min to allow for equalization and charging of the accumulator. This pressure corresponds to the volume required (≈100 μL) to create a 1 mm thick coating. An inline crimp valve was then closed to isolate the accumulator from the pressure source. The stopper tool was then removed, allowing the valve to open and release of the healing agent. For subsequent generations (1–4), the system was charged with 97 kPa pressure and equilibrated for 1 min, then a small razor blade was used to remove the cured coating from the substrate. The pressure was allowed to decay for 3 min (sufficient time to be in the plateau region, $p = p_{close}$, Figure 5), at which time the specimen was removed from the stage and the pressure source. The coating was then cured under UV light for 12 h (1 mW cm^{-2}, 365 nm peak wavelength). The diameter and thickness of each generation of coating was measured. Hardness of the coating was measured using a Vickers indentation hardness tester (5 measurements, 50 g, 5 s, HMV-M3, Shimadzu).

Article first published online: xxxx
Manuscript Revised: May 11, 2017
Manuscript Received: April 6, 2017

[1] B. J. Blaiszik, S. L. B. Kramer, S. C. Olugebefola, J. S. Moore, N. R. Sottos, S. R. White, *Annu. Rev. Mater. Res.* **2010**, *40*, 179.
[2] Y. Yang, M. W. Urban, *Chem. Soc. Rev.* **2013**, *42*, 7446.
[3] Y. C. Yuan, T. Yin, M. Z. Rong, M. Q. Zhang, *Express Polym. Lett.* **2008**, *2*, 238.
[4] A. R. Hamilton, N. R. Sottos, S. R. White, *J. R. Soc. Interface* **2012**, *9*, 1020.
[5] H. R. Williams, R. S. Trask, I. P. Bond, *Compos. Sci. Technol.* **2008**, *68*, 3171.
[6] S. R. White, J. S. Moore, N. R. Sottos, B. P. Krull, W. A. Santa Cruz, R. C. R. Gergely, *Science* **2014**, *344*, 620.
[7] S. H. Cho, S. R. White, P. V. Braun, *Adv. Mater.* **2009**, *21*, 645.
[8] K. S. Toohey, N. R. Sottos, J. A. Lewis, J. S. Moore, S. R. White, *Nat. Mater.* **2007**, *6*, 581.

[9] J. F. Patrick, K. R. Hart, B. P. Krull, C. E. Diesendruck, J. S. Moore, S. R. White, N. R. Sottos, *Adv. Mater.* **2014**, *26*, 4302.
[10] X. Chen, M. A. Dam, K. Ono, A. Mal, H. Shen, S. R. Nutt, K. Sheran, F. Wudl, *Science* **2002**, *295*, 1698.
[11] P. Cordier, F. Tournilhac, C. Soulié-Ziakovic, L. Leibler, *Nature* **2008**, *451*, 977.
[12] R. C. R. Gergely, N. R. Sottos, S. R. White, *Adv. Eng. Mater.* in press (DOI: 10.1002/adem.201700308).
[13] P. Froimowicz, H. Frey, K. Landfester, *Macromol. Rapid Commun*. **2011**, *32*, 468.
[14] B. Ghosh, M. W. Urban, *Science* **2009**, *323*, 1458.
[15] J. Ling, M. Z. Rong, M. Q. Zhang, *Polymer (UK)* **2012**, *53*, 2691.
[16] H. Zhang, D. Han, Q. Yan, D. Fortin, H. Xia, Y. Zhao, *J. Mater. Chem. A* **2014**, *2*, 13373.
[17] C. M. Chung, Y. S. Roh, S. Y. Cho, J. G. Kim, *Chem. Mater.* **2004**, *16*, 3982.
[18] S. Ji, W. Cao, Y. Yu, H. Xu, *Adv. Mater.* **2015**, *27*, 7740.
[19] M. V. Biyani, E. J. Foster, C. Weder, *ACS Macro Lett*. **2013**, *2*, 236.
[20] R. Schwalm, *UV Coatings: Basics, Recent Developments and New Applications*, Elsevier, Amsterdam **2007**.
[21] N. B. Cramer, C. L. Couch, K. M. Schreck, J. E. Boulden, R. Wydra, J. W. Stansbury, C. N. Bowman, *Dent. Mater.* **2010**, *26*, 799.
[22] H. Lu, J. A. Carioscia, J. W. Stansbury, C. N. Bowman, *Dent. Mater.* **2005**, *21*, 1129.
[23] P. F. Jacobs, *Sterolithography and Other RP&M Technologies*, Society of Manufacturing Engineers, Dearborn, MI, **1996**.
[24] J. T. Cabral, S. D. Hudson, C. Harrison, J. F. Douglas, *Langmuir* **2004**, *20*, 10020.
[25] J. T. Cabral, J. F. Douglas, *Polymer* **2005**, *46*, 4230.
[26] K.-H. Jeong, G. L. Liu, N. Chronis, L. P. Lee, *Opt. Express* **2004**, *12*, 2494.
[27] E. W. Weisstein, "Spherical Cap," http://mathworld.wolfram.com/SphericalCap.html, accessed: March **2016**.
[28] A. N. Gent, *Rubber Chem. Technol*. **1999**, *72*, 263.
[29] R. Mangan, M. Destrade, *Int. J. Non Linear Mech*. **2015**, *68*, 52.
[30] H. H. Bednar, *Pressure Vessel Design Handbook*, Van Nostrand Reinhod Company, New York, NY **1981**.
[31] A. N. Gent, *Rubber Chem. Technol*. **1969**, *96*, 59.
[32] R. W. Ogden, *Proc. R. Soc. A Math. Phys. Eng. Sci*. **1972**, *326*, 565.
[33] Specimen #1 failed during recharge for generation 4 due to rupture of the accumulator. In addition, the coating material became more difficult to lift from the substrate during removal of generations 2 and 3 (formation of generations 3 and 4) causing breakup of the coating and some material to remain attached to the substrate. As a consequence, during generation 3 of specimen #2, we were unable to remove the coating using the described liftoff and triggered release method. Instead the coating was removed while the specimen was uncharged, and the coating was regenerated as in generation 0. Furthermore, coating removal resulted in some transfer of healing agent from the specimen, which leads to lower than expected coating thickness.
[34] A. M. Coppola, A. S. Griffin, N. R. Sottos, S. R. White, *Compos. Part A Appl. Sci. Manuf*. **2015**, *78*, 412.
[35] R. F. Shepherd, F. Ilievski, W. Choi, S. A. Morin, A. A. Stokes, A. D. Mazzeo, X. Chen, M. Wang, G. M. Whitesides, *Proc. Natl. Acad. Sci. USA* **2011**, *108*, 20400.
[36] V. P. Rajan, M. N. Rossol, F. W. Zok, *Exp. Mech*. **2012**, *52*, 1407.